Millimeter-Wave Imaging Sensor

WILLIAM J. WILSON, SENIOR MEMBER, IEEE, R. J. HOWARD, MEMBER, IEEE, ANTHONY C. IBBOTT, GARY S. PARKS, AND WILLIAM B. RICKETTS

Abstract—**A scanning 3-mm radiometer system has been built and used on a helicopter to produce moderate-resolution (0.5°) images of the ground. This millimeter-wave sensor can be used for a variety of remote-sensing applications and produces images through clouds, smoke, and dust when visual and IR sensors are not usable. The system is described and imaging results are presented.**

I. INTRODUCTION

A 3-MM RADIOMETER SYSTEM with a mechanically scanned antenna has been built for use on a small aircraft or helicopter to produce near-real-time, moderate-resolution images of the ground. One of the main advantages of this passive imaging sensor is that it is able to provide information through clouds, smoke, and dust when visual and IR systems are unusable. This millimeter-wave imaging sensor can also be used for a variety of remote-sensing applications, such as measurements of snow cover, surface moisture, vegetation type and extent, mineral type and extent, and surface temperature and thermal inertia. It is also possible to map fires and volcanic lava flows through obscuring clouds and smoke. The fact that the millimeter-wave sensor observes different physical phenomena makes it a valuable addition to visual and IR imaging systems.

When a millimeter-wave radiometer observes a ground scene from above, as shown in Fig. 1, the received signal temperature is composed of emission from objects in the antenna beam, reflected sky emission, and atmospheric emission from the atmosphere below the radiometer

$$T_{\text{received}} = T_{\text{object}} + T_{\text{background}} + T_{\substack{\text{reflected}\\ \text{sky}}} + T_{\text{atmos}}(\text{K}). \quad (1)$$

To simplify the equations, it has been assumed that all of the received power is within the main antenna beam, which is defined by the half-power beamwidth Θ_b. (This is a good assumption for the antennas with beam efficiencies of > 90 percent used in imaging systems.)

The received temperature from an object in the antenna beam is equal to the product of the object's temperature and its emissivity, multiplied by the ratio of the object's area to the antenna's beam area and reduced by the atmospheric attenuation

$$T_{\text{object}} = \frac{\epsilon T \eta}{L_a}(\text{K}) \quad (2)$$

where

- ϵ emissivity of the object ($0 \leqslant \epsilon \leqslant 1$),
- T physical temperature of the object (K),
- L_a atmospheric absorption factor below the radiometer, i.e., $10^{(L_{\text{atm}} \cdot R/10^4)}$,
- L_{atm} atmospheric attenuation (dB/km) below the radiometer,
- R range to object (m),
- η ratio of objects area to main beam area ($0 \leqslant \eta \leqslant 1$), i.e., $A/(\pi/4)(R \tan \Theta_b)^2$,
- A object's area (m^2).

The reflected sky emission temperature is equal to the product of the radiometric sky temperature and the quantity $(1-\epsilon)$ and is also multiplied by the ratio of the object's area to the antenna's beam area and reduced by the atmospheric absorption

$$T_{\substack{\text{reflected}\\ \text{sky}}} = \frac{(1-\epsilon) T_{\text{sky}} \eta}{L_a}(\text{K}) \quad (3)$$

where

T_{sky} radiometric sky temperature,

$$\cong T_{\text{atm}}\left(1 - \frac{1}{L_z}\right) + \frac{T_{\text{cb}}}{L_z}(\text{K}),$$

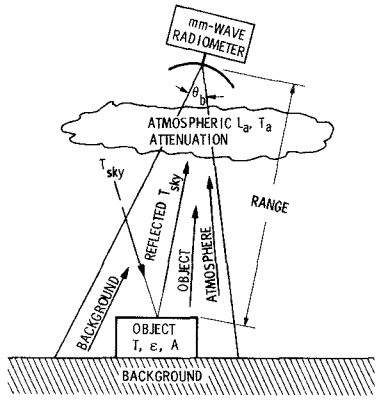

Fig. 1. Millimeter-wave radiometer observing a ground scene from above.

Manuscript received March 3, 1986; revised June 5, 1986.
The authors are with the Jet Propulsion Laboratory, Pasadena, CA.
IEEE Log Number 8609962

TABLE I
RECEIVED SIGNAL TEMPERATURES FOR VARIOUS ATMOSPHERIC CONDITIONS WHEN OBSERVING AN OBJECT ($T = 290$ K) WHICH FILLS THE ANTENNA BEAM ($\eta = 1$) FROM A RANGE OF 750 METERS

Atmospheric Conditions (T_a = 290 K) (Attenuation at 98 GHz)	T_{sky}	$T_{received}$	
		ϵ = 0.1	ϵ = 0.8
Clear, Smoke, Light Fog (L_{atm} = 0.6 dB/km)	60 K	103 K	249 K
Thick Fog, Overcast (L_{atm} = 1.0 dB/km)	120 K	161 K	261 K
Thick Clouds (L_{atm} = 2.0 dB/km)	180 K	220 K	274 K

T_{atm} mean atmospheric temperature ($\cong$ 280 K),
L_z total zenith absorption factor,
T_{cb} cosmic background radiation temperature (= 2.7 K).

The received signal temperature from the background surrounding the object is given by

$$T_{\text{background}} = \left(\frac{\epsilon_g T_g + (1-\epsilon_g) T_{\text{sky}}}{L_a} \right) (1-\eta) \qquad (4)$$

where ϵ_g is the emissivity of the background and T_g is the physical temperature of the background. The atmospheric emission below the radiometer is

$$T_{\text{atmos}} = T_a \left(1 - \frac{1}{L_a} \right) \qquad (5)$$

where T_a is the physical temperature of the atmosphere below the radiometer.

The received signal temperatures under various atmospheric conditions for a reflective object with low emissivity ($\epsilon = 0.1$) and for an absorbing object with high emissivity ($\epsilon = 0.8$) are shown in Table I. In this table, it was assumed that the object fills the beam ($\eta = 1$) and is observed from a range of 750 m. For the atmospheric conditions in Table I, reflective objects (metal or water) will appear colder than the surrounding high-emissivity background (soil or vegetation); thus, reflective objects will "stand out" from the surrounding background with a large temperature difference or signal-to-noise ratio. In the design of a small millimeter-wave sensor for the detection of small reflective objects in *cloudy weather*, it was determined that the 98-GHz atmospheric window provided the best signal-to-noise ratio of any frequency. At the higher frequency windows (140 and 220 GHz), the gain from the smaller antenna beamwidth Θ_b was canceled by the larger atmospheric attenuation in cloudy weather.

In Section II, descriptions of the systems for the millimeter-wave imaging sensor are presented. Section III discusses the results from the initial test program.

II. SYSTEM DESCRIPTION

A. Overall System

The system configuration is shown in Fig. 2, and the system block diagram is shown in Fig. 3. A lightweight flat reflector is mechanically scanned cross-track ± 20 degrees at a 4-Hz rate. A two-axis scanner, controlled by a microcomputer with inputs from both rate and angle gyros, is used to scan the reflector and to correct for aircraft movement due to turbulence. This provides line-of-sight stabilization without the use of a conventional stabilized platform. The two-axis scanner also uses a butterfly scanning pattern to compensate for the forward aircraft motion to produce a linear raster scan pattern on the ground. A 0.1° pointing stability is achieved to eliminate pixel smear and image distortion. The signal from the ground is reflected from the flat scanning mirror onto a 16-in offset parabolic antenna, which focuses the received signal on the radiometer's feed horn. An offset parabolic antenna was designed and used for its high beam efficiency ($\eta_b > 0.9$) and low sidelobes [5], [6].

Two linearly polarized (horizontal and vertical) 98-GHz superheterodyne radiometers were used to provide polarization information and to improve the measurement sensitivity. The radiometers use balanced mixers with beam-lead diodes. A single Gunn diode local oscillator is used for both radiometers. The rms noise per ground resolution element is < 0.8 K when both channels are added. A calibrated signal is injected into the feed horn at the end of each scan line to provide temperature calibration. In addition, an ambient load is placed over the feed on command to provide additional calibration. The relative accuracy is ± 1 K, and the absolute accuracy is ± 10 K.

The output signals from the radiometers are digitized, converted to a brightness temperature, and recorded on a digital cartridge tape by a microcomputer. Ground truth data are given by a 35-mm camera and a video camera which are used to record visual scene data. Because the data are taken with a stabilized raster pattern, the ground computer system can immediately display the data in false colors on a video monitor. The features which make this

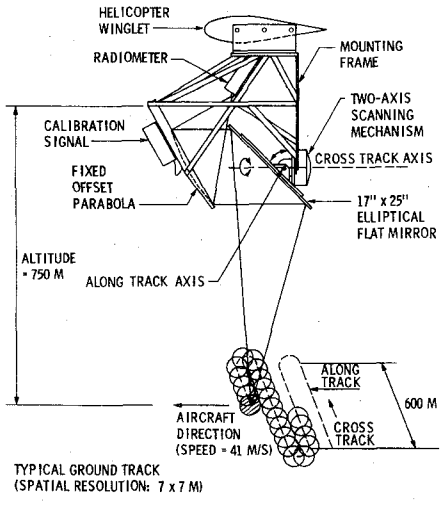

Fig. 2. Millimeter-wave imaging sensor configuration.

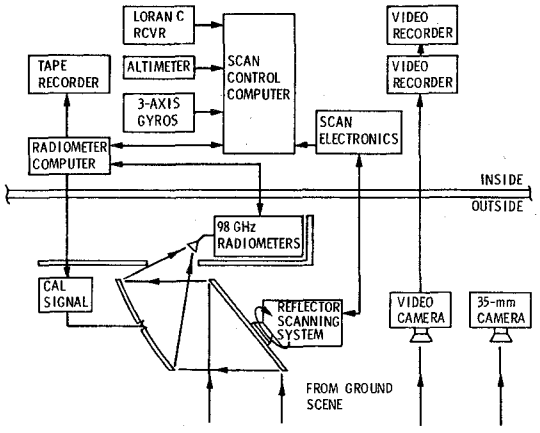

Fig. 3. Millimeter-wave imaging sensor system.

system unique from previous airborne millimeter-wave imaging sensors [1]–[4] are its high resolution, small size, stabilization, and computer processing to provide near-real-time calibrated images.

B. Antenna

The requirements for the antenna system are a 0.5° antenna beam with a main beam efficiency greater than 90 percent. The antenna system consists of a scanning elliptical flat reflector, a fixed offset parabolic reflector, and a feed horn. The optics configuration is shown in Fig. 2, and a photograph of the assembled antenna system and scanner is shown in Fig. 4.

The scanning 17×25-in elliptical reflector was made from 1/2-in aluminum honeycomb sandwich material with 0.020-in-thick aluminum facing. The reflector was epoxyed to the mounting bracket of the scanner and then temperature cycled to relieve mechanical stresses. The weight of the reflector with the bracket is 3.5 lb. The front surface was then lapped to achieve the required flatness. The rms deviation from a plane of the final surface was measured and found to be 0.0009 in.

The fixed offset parabola was designed with an F/D ratio of 0.300 and a focal distance (F) of 13.680 in. A

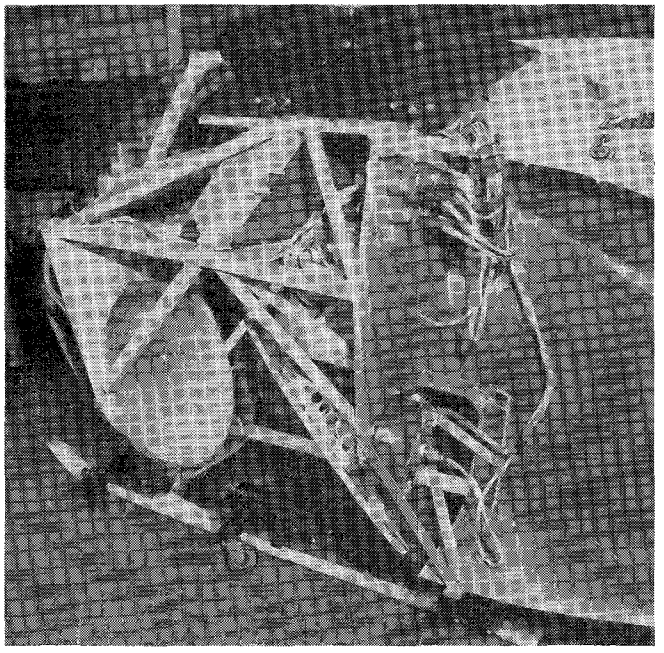

Fig. 4. Photograph of the assembled antenna and scanning system, mounted on the helicopter winglet.

1-in-diameter hole in the center of the parabola was used for injecting the calibration signal into the radiometer feed horn. After the parabolic surface was temperature cycled to relieve any mechanical stresses, the rms surface errors from the design parabola were found to be 0.0012 in. The scalar feed horn was designed to have a 16-dB illumination taper with its first sidelobes 28 dB down from peak power. The feed beam efficiency is 97 percent for the angle subtended by the parabola (51.7°).

The overall antenna beam efficiency was estimated using the following relationship:

$$\eta_b = \eta_h \quad \eta_{bl} \quad \eta_p \quad \eta_f \quad \eta_w \tag{6}$$

where

- η_h feed horn beam efficiency (= 0.97),
- η_{bl} blockage efficiency of the optics system (= 0.99),
- η_p parabola efficiency due to surface errors (= 0.99),
- η_f elliptical flat efficiency due to surface errors (= 0.99),
- η_w transmission efficiency of the window material (= 0.97).

The only contribution to the blockage efficiency η_{bl} is the central hole in the parabola, which reduces the antenna beam efficiency by ≈1 percent and increases the antenna sidelobes by ≈ 2 dB. The shroud window material is a piece of Griffolyn T55 stretched over a metal frame. Griffolyn T55 is a nylon-reinforced plastic fabric which is strong and yet has loss < 0.1 dB at millimeter wavelengths. Using these values, the calculated beam efficiency η_b is 0.91, which is in good agreement with the measured value of 0.89. Measurements of the beam shape and sidelobe levels determined that the beam shape was symmetric with a half-power beamwidth of ~0.5°, with the first sidelobe levels 23–26 dB down from the on-axis power.

Data were taken over a $\pm 5°$ area from the main beam direction, and no other sidelobes were detected to a level of > 30 dB below the on-axis power.

C. Scanner

The two-axis scanner, which moves the 17×25-in flat reflector, was designed and built to JPL specifications by the Sperry Corporation in Phoenix, AZ. The scanner was designed to scan the reflector $\pm 22.5°$ cross-track following a 4-Hz triangular waveform. The scanner cross-track response was designed to be linear for 75 percent of the cycle with a maximum turnaround time of 30 ms. At the same time, the along-track axis was designed to follow an 8-Hz sawtooth waveform with 0.4° amplitude to compensate for the forward velocity of the aircraft. To compensate for aircraft motions, the scanner is also required to follow these waveforms over an angular roll range of $\pm 15°$ for the cross-track axis and $\pm 10°$ for the along-track axis.

To follow these signals, the cross-track frequency response was required to have a 3-dB bandwidth of 55 Hz, while the along-track bandwidth was 30 Hz. These bandwidths are also consistent with a stabilization lag requirement of less than 10 ms in cross-track and 20 ms in the along-track axis. Angle encoders were used to measure the position of each axis to an accuracy of 0.1°. The short-term ($\leqslant 2$ min) repeatability of the scanner is 0.2° in the cross-track axis and 0.1° in the along-track axis.

D. Stabilization

The requirement for the stabilization system is to stabilize the antenna half-power beamwidth to within $\Theta_b/5 = 0.1°$ from the aircraft motions. The aircraft motions will have a random frequency spectrum up to 2 Hz and maximum angular rates of $\pm 10°/s$ with a maximum angular change of $\pm 7°$. With the two-axis scan system, the stabilization corrections are superimposed on the raster motions which are required for the millimeter-wave imaging.

Because of the raster scanning motions, the angular motion sensors (rate and position gyros) are mounted to the fixed antenna structure, and an open/closed loop concept is used to drive the reflector pointing in a direction opposite the frame motion. Because of their higher frequency response, rate gyros are used open loop for a fast stabilization correction. A vertical gyro is used in a closed loop for the slow frequency reference.

The entire stabilization loop is processed by a 16-bit microcomputer. Only the gyros and scanner electronic control are not computer stabilization functions. The scan computer throughput time is 10 ms, and a resettable hardware integrator is used to command the scanner between computer cycles. Control of this system, via software, made achievement of the required performance straightforward.

E. Radiometer and Calibration

The radiometer consists of two superheterodyne mixer receivers. A block diagram of the radiometer is shown in Fig. 5. A broad-band orthomode junction splits the received signal into two orthogonal, linearly polarized signals. Balanced beam-lead diode mixers are used to convert the RF signal down to an IF signal centered at 3 GHz with a 2-GHz bandwidth. A Gunn diode oscillator, tuned to 98 GHz and split with a hybrid tee, is used to provide 2 mW of local oscillator power for each mixer. Each mixer is followed by a low-noise (1.5-dB noise figure) GaAs FET amplifier. This mixer–preamp combination has an RF-to-IF gain of 34 dB and a double sideband (DSB) noise temperature of < 750 K, measured at the mixer input. The measured DSB receiver temperatures, referenced to the feed horn, are 850 K and 1050 K for each receiver. The IF components following the mixer–preamp consist of another GaAs FET amplifier, a voltage-controlled pin diode attenuator, and a bandpass filter centered at 3 GHz with a 3-dB bandwidth of 2100 MHz. Following these components, a tunnel diode detector is used to convert the IF power to a dc voltage. A photograph of the assembled radiometer is shown in Fig. 6.

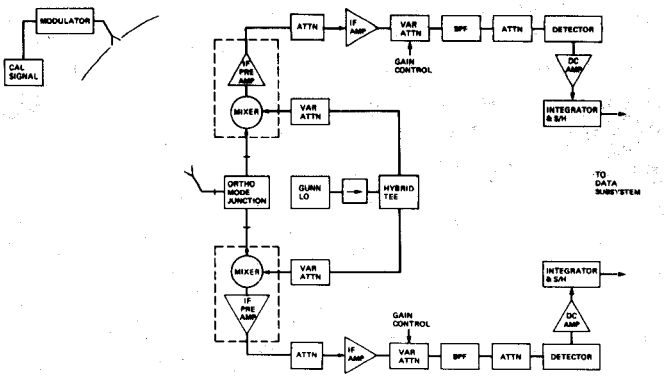

Fig. 5. Dual polarization 98-GHz radiometers and calibration system.

Fig. 6. Photograph of the assembled dual polarized 98-GHz radiometers. The chassis size is $14 \times 9 \times 3$-in.

The radiometer box was temperature stabilized to within $\pm 2°C$ to reduce gain variations and to keep the receiver noise temperature constant. The output signal from each detector was amplified, integrated for ~ 0.5 ms, and then sampled with a sample-and-hold circuit. The signal was sampled at an interval corresponding to every one-half beamwidth on the ground. The sampled output signal was then sent to the radiometer computer, where it was digitized and converted to a brightness temperature.

Each radiometer is calibrated during the scanner's turnaround time at the end of each data line, which provides a calibration of the receiver gain every 125 ms. During the calibration period (~ 30 ms), the output of the 95-GHz Gunn diode calibration oscillator is modulated by the data system at ~1000 Hz and transmitted from the calibration box, through the central hole in the offset parabola, to the radiometer. This calibration signal is in the lower sideband of the radiometers; however, it was calibrated with thermal loads which have power in both sidebands. The calibration signal is polarized at a 45° angle to the radiometers' polarizations to provide nearly equal signals for each radiometer. The calibration box is temperature stabilized to within ±1°C to stabilize the calibration signal strength. The radiometer computer measures the calibration "ON–OFF" data and calculates a new gain based on a measured calibration temperature according to the formula

$$G = \frac{\sum^{n} (V_{\text{cal ON}} - V_{\text{cal OFF}})}{n\, T_{\text{cal}}} \tag{7}$$

where

G radiometer gain (V/deg K),
$V_{\text{cal ON}}$ voltage out of the radiometer when the cal signal was on,
$V_{\text{cal OFF}}$ voltage out of the radiometer when the cal signal was off,
n number of ON–OFF pairs during the calibration sequence ($n = 30$),
T_{cal} measured temperature of the cal signal using ambient and liquid nitrogen loads (≈150 K).

The radiometer computer calculates a running average of 100 of these gain values and uses this average gain $\bar{G}$ in computing the scene temperatures.

Once a minute, during the scanner turnaround, the radiometer computer turns off the radiometer, using the voltage-controlled IF attenuator, and measures the zero RF power output V_z of the radiometer. A running average of seven zeros $\bar{V}_z$ is used in the calculations.

With $\bar{G}$ and $\bar{V}_z$ calculated, the scene temperatures are derived from the sampled radiometer voltage output V. The first step is to calculate the system noise temperature (T_{sys}) using the expression

$$T_{\text{sys}} = \frac{(V - \bar{V}_z)}{\bar{G}}. \tag{8}$$

The system noise temperature is also equal to

$$T_{\text{sys}} = \eta_b T_{sc} + T_r + (1 - \eta_b) T_{\text{amb}} \tag{9}$$

where

η_b antenna beam efficiency = 0.90,
T_{amb} temperature at which all power outside the main beam is terminated (≈ 295 K),
T_r receiver DSB noise temperature measured using ambient and liquid nitrogen loads,
T_{sc} radiometric scene temperature of the area within the main beam.

Since η_b, T_r, and T_{amb} are known, the scene temperature can be calculated

$$T_{sc} = \frac{T_{\text{sys}} - (1 - \eta_b) T_{\text{amb}} - T_r}{\eta_b}. \tag{10}$$

Since the actual system noise temperatures are between 1000°K and 1250°K for typical scenes, a small change in the calibration signal level will change the calculated scene temperature by a large amount. For example, with a calibration level change of only 5 percent, a 50-K scene would appear to be 107 K. To improve the absolute accuracy of the system, an additional calibration point was used. Under operator control, an ambient vane absorber is positioned in front of the radiometer feed about every 15 min. The radiometer computer continues to take data but with no calibrations for ~ 5 s, and after 5 s the vane is removed from the beam. The physical temperature of the vane (T_v) is monitored and recorded on the data tape. Assuming that $T_v = T_{\text{amb}}$ and that T_r is constant when the data are processed by the ground computer to obtain the observed scene temperature of the vane ($\bar{T}_v$), a new gain G' can be calculated using the following relationship:

$$\frac{G'}{\bar{G}} = \frac{\bar{T}_v + T_r}{T_v + T_r}. \tag{11}$$

Using this technique to correct the gains after the fact, the absolute accuracy of the scene temperature is estimated to be ±10 K over the entire range of temperatures. For many scenes, the hottest areas will be ≈ T_{amb}; thus, each scene's temperature level can be adjusted further in the data reduction. With the frequent gain calibrations, the relative temperature accuracy is good and for temperatures in the 200–300-K range, the absolute data calibration is estimated to be ±5 K.

F. Aircraft Computers

The scan microcomputer is required to control the scanner to scan the beam in a linear raster pattern on the ground, free from disturbances caused by aircraft attitude motions. This includes the linear scanning cross-track motion, the along-track reverse motion to compensate for the aircraft forward velocity, and signals to stabilize the line-of-sight pointing, as discussed in Section II-D. In addition, this computer is also used to correct for nonlinear scanner response versus frequency and for an undesirable cross-coupling between the cross-track and along-track scanner motions. The scan computer also controls the timing for the radiometer data acquisition and for the calibration during scanner turnaround.

A separate microcomputer is used to acquire and process the radiometer data. This computer controls radiometer integration times, reads the sampled radiometer data, and converts these data to brightness temperatures utiliz-

ing the real-time calibration data. This output is recorded on the cartridge magnetic tape. Ancillary data from aircraft instruments, such as aircraft position, heading, and altitude, are also recorded on tape.

The microcomputer performance requirements are as follows:

a) 32-bit floating point capability;
b) 10-ms stabilization coordinate conversion, which requires 200 000 floating point operations per second;
c) 16-bit integer operations in less than 1 μs;
d) multiple level (> 4) interrupt capability (multitasking);
e) small, lightweight (< 20 lb) and able to survive a typical aircraft vibration environment;
f) analog and digital I/O capability.

The requirements listed above indicate a need for a powerful and fast microprocessor system. Typical 8-bit processors would be as much as 10 times too slow for the required task; therefore, dual 16-bit Motorola-68000-based computers were chosen. This scheme allows the parallel processing of radiometer data and scanner control which is required by the system.

The system block diagram, in Fig. 3, shows the aircraft computers and interfaces to other equipment. The radiometer computer has seven boards, most of which are I/O. The single-board computer consists of the 68000 CPU, memory (RAM and ROM), a timer for time-critical operations, and associated control electronics. The program resides in read only memory (ROM) and has access to enough random access memory (RAM) for computations and storage. A 256 K RAM board, along with the general-purpose interface bus (GPIB) board, allows direct memory access capability, which in turn allows tape operations to be done completely in parallel with, and independent of, CPU operations. Similarly, the scan control computer consists of six boards, including the CPU board, I/O, and a floating point processor for stabilization processing. The signal conditioning board commands the gimbal between stabilization computer command loops and also conditions aircraft instrument signals.

G. Ground Computer System

The millimeter-wave image processing hardware consists of an HP A-700 computer with a video interface board, a CRT display terminal, a printer, a cartridge tape drive, and a CONRAC RGB color monitor. The computer reads data from a source tape in the cartridge tape drive unit and displays the images on the color monitor. Numeric log information can be sent to the printer, and a camera is used to make hard copies of the images.

The software processing functions are controlled by menus. This allows imaging of either radiometer channel, their sum or difference, and specifies offsets and scale factors. The displayed temperature range and the false color image map can also be selected. There are two modes of image display: the first displays three columns consisting of approximately 3 min of data at a time, and the second displays enhanced images of 20 s of scene segments. In the enhanced mode, a scene is selected and displayed in one screen quadrant along with a color histogram of the scene temperatures. The temperature range and colors can be adjusted and the scene redisplayed in an adjacent screen quadrant. The enhanced mode also allows for smoothing, edge enhancement, and a zoom capability.

Fig. 7. Photograph of the millimeter-wave imager in the shroud, mounted on the winglet, on a Bell Jet Ranger helicopter. The 35-mm camera is mounted on the opposite side and the video camera is mounted in front.

III. Results

The first test flights of the millimeter-wave imager were made in September 1985 with the sensor mounted on a commercial helicopter as shown in Fig. 7. All flights were near an altitude of 750 m (2500 ft) above ground level and at an air speed of ~ 90 km/h (~ 56 mph). The objectives of these test flights were to verify the capabilities of this sensor (with respect to signal to noise and operation with clouds) and to obtain millimeter-wave imaging data on a variety of scenes of cities, highways, farmland, water, and ships. Fourteen test flights were made between September 13 and 26, 1985, to accomplish these objectives. These tests were very successful and samples of the data are shown in Figs. 8–12.

Images of a city and a freeway near Simi Valley, CA, are shown in Fig. 8. Both the millimeter-wave data and the visual video data are shown for easier interpretation. The coldest objects are the metal objects, which have a brightness temperature of ~ 75 K. The hottest objects are at the ambient temperature of 300 K. This scene clearly shows the freeway, its intersections, and the adjacent houses. Many of the vehicles on the roads in the visual image are shown in the millimeter-wave image, and position differences are mainly due to the slightly different times of the video and millimeter-wave images. The speed of the helicopter was faster than the traffic; thus, vehicles moving in the same direction are stretched because of more scans

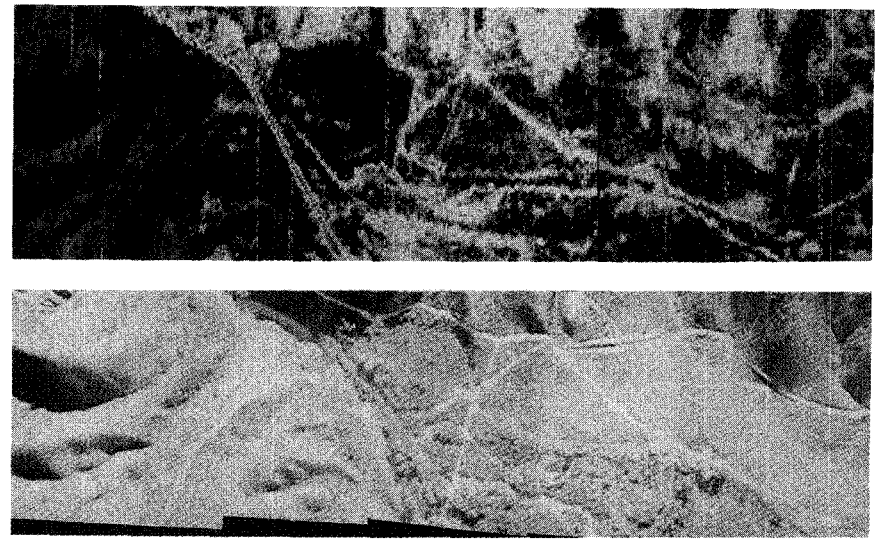

Fig. 10. Video and millimeter-wave images of an area northeast of that in Fig. 9 of barren land showing hills with shadows. The flight parameters and color scale are identical to those in Fig. 9. See the text for a discussion of these data.

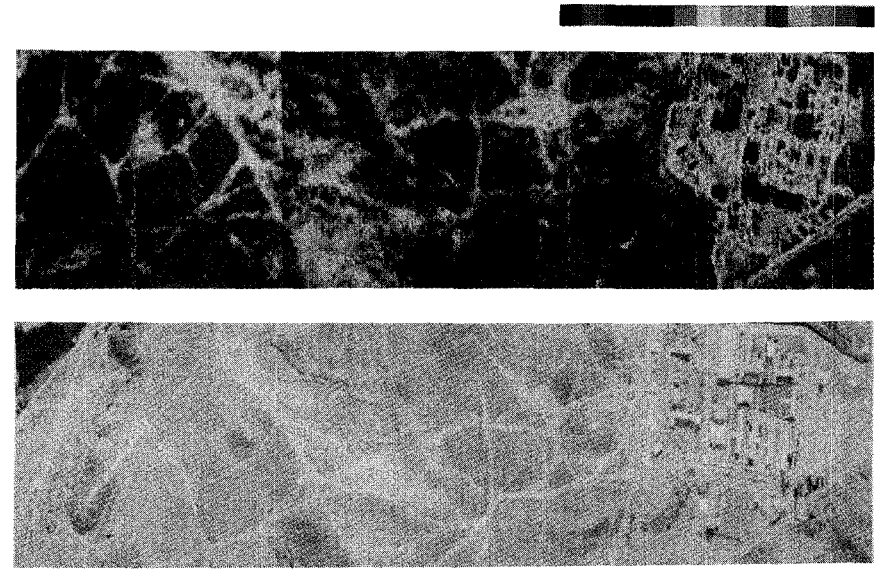

Fig. 9. 35-mm and millimeter-wave images of an area near Carlsbad, CA, on Sept. 22, 1985, showing a complex of buildings, parking lots with vehicles, and barren land beyond. The 15-level color scale is from 250 K (dark blue) to 300 K (red). The scene width is 0.5 km and the length is 1.3 km.

Fig. 8. Video and millimeter-wave images of a freeway scene near Simi Valley, CA, on Sept. 13, 1985. The 15-level color scale is from 250 K (dark blue) to 300 K (red). The scene width is 0.55 km with 173 data pixels across and the length is 2.1 km.

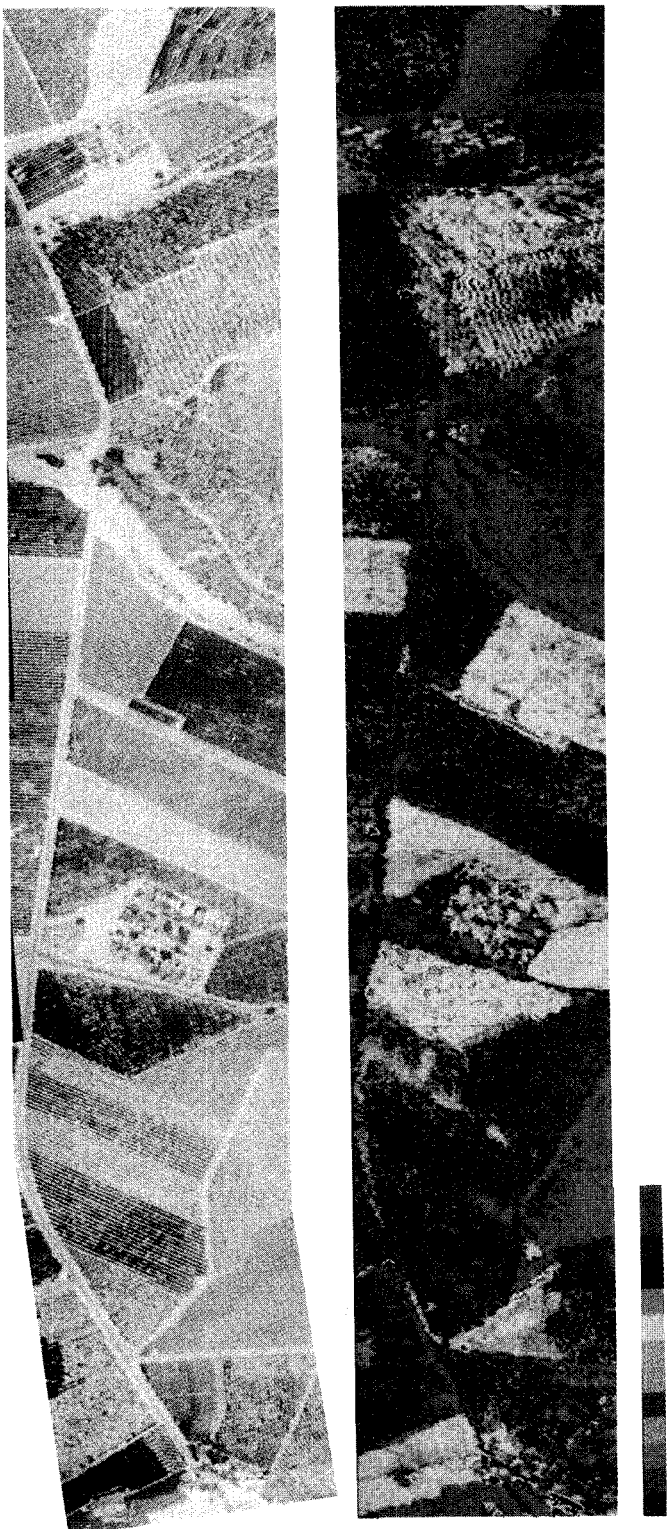

Fig. 11. Video and millimeter-wave images of a citrus agricultural area west of Fillmore, CA. The cold areas in the fields are water and wet soil from irrigation. The color scale is identical to Fig. 9. The scene width is 0.6 km and the length is 2.3 km.

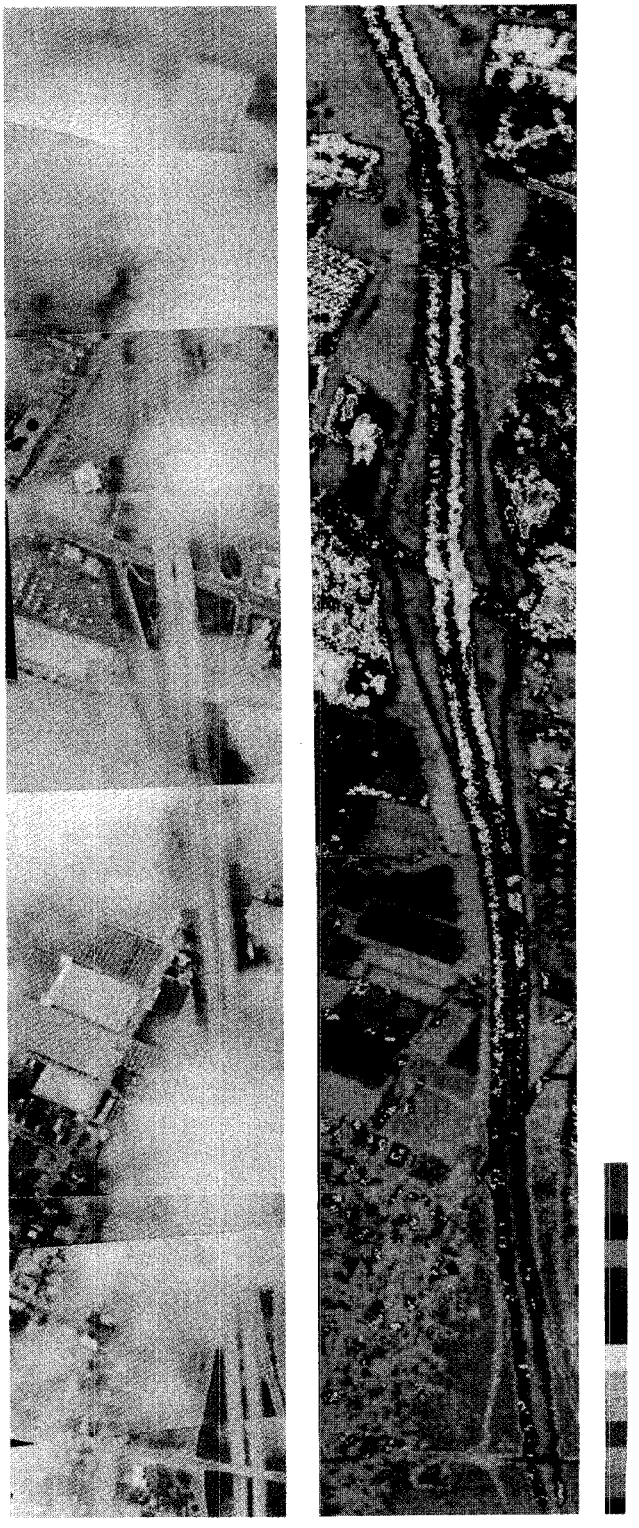

Fig. 12. Video and millimeter-wave images of a freeway scene south of Carlsbad, CA, on Sept. 26, 1985. During this rainy day, the sensor was flown over a layer of broken clouds, as seen in the pictures from the video. The color scale is identical to Fig. 8. The scene width is 0.4 km and the length is 1.9 km.

on the vehicle, while vehicles moving in the opposite direction are compressed or missed completely. Numerous swimming pools, which are not obvious in the visual image, can be seen in the backyards of houses on the left side of the freeway. Enough of the millimeter-wave features are recognizable so that it is very easy to correlate it with the visual data.

In Figs. 9 and 10, the visual and millimeter-wave images of a coastal area near Carlsbad, CA, are shown. The buildings, parking lots, and cars in the lower portion of Fig. 9 appear much colder due to their higher reflectivity. Some roads are also seen due to emissivity differences between them and the rougher land. If a lower range of temperatures is displayed, all the rows of vehicles in the parking lots are easily seen, and there is much more detail shown in this complex of buildings. In the top part of the visual photograph in Fig. 10 are shown hills with shadows. These data were taken at 0823 h, and the millimeter-wave image clearly shows the cooler temperatures in the shadows. The asphalt road in the center of the image is ~ 15 K cooler than the surrounding background, and there are two vehicles detected on this road. The cold objects in the lower portion are concrete pads and metal storage tanks, and there is even a detection of a power line across the middle section of Fig. 10.

Millimeter-wave and visual images of an agricultural area west of Fillmore, CA, are shown in Fig. 11. Most of the trees in this area are citrus, and there is a dry river bed near the top of the image. All the fields are clearly outlined, and the cold areas in the fields are standing water and wet soil from irrigation. In the false-color images, where this water really stands out, it is very easy to see where the irrigation water has reached. The coldest areas are storage tanks, vehicles, and buildings. The warmest areas are ploughed fields and the dry river bed. Differences in the millimeter-wave image of several fields are apparent due to differences in the vegetation or soil moisture, while the visual picture was uniform.

Fig. 12 shows the visual and millimeter-wave images of the freeway south of Carlsbad, CA, on September 26, 1985, during a rainy day. During this day, the millimeter-wave sensor was flown at 2500 ft over a layer of broken clouds, which completely obscured the visual images over large areas. On the millimeter-wave image, the freeways, vehicles, parking lots, and buildings are clearly shown as colder targets, reflecting the cooler sky. As in Fig. 8, vehicles on the freeway traveling in the same direction as the helicopter have been stretched, while those traveling in the opposite direction have been compressed. This picture clearly shows the ability of the millimeter-wave imager to provide information on the ground scene when the video image is obscured by the clouds.

IV. Conclusions

One of the most interesting things about these millimeter-wave images is that there are many recognizable objects; i.e., reflective objects, such as water, metals, highways, and buildings, which stand out from the background "clutter." From a study of many images, it is rare that the temperature range needs to be expanded beyond 3 K per color step, which is ~ 4 times larger than the radiometer noise, since the scene "clutter" is between 2–3 K. It is also interesting that, by properly choosing the range of temperatures and the order of colors, different features within a scene can be made to "stand out" or "blend in" the picture. Other image processing and enhancement techniques can also be used to improve object detection.

Images with important features can be made day or night and through smoke, fog, and clouds when IR and visual sensors are not usable. From the measurements of the signal to noise ratio in the images produced through clouds, the expected performance was verified, thus allowing predictions for using the sensor in degraded weather conditions. Using a passive millimeter-wave imaging sensor for surveillance will be one of its best applications. Other remote sensing applications, as mentioned in the introduction, may also turn out to be important, and the data are now being analyzed to determine the usefulness of the imager in these applications.

Millimeter-wave technology has allowed us to build a reliable, solid-state, low-noise, dual-channel 98-GHz radiometer in a $14 \times 9 \times 3$-in chassis; however, it is the powerful computer technology, which controls the scanner, calibration, and radiometer data and then can quickly display the final images, that makes this millimeter-wave imager so unique and useful. One of the most important future developments for this system would be to reduce its size for use on smaller aircraft. This will require the development of a 100-GHz electronic scanning antenna or a cross-track antenna array with multiple receivers. Small integrated receivers would also be advantageous for future millimeter-wave imaging systems.

References

[1] J. P. Hollinger, J. E. Kenney, and B. E. Troy, Jr., "A versatile millimeter-wave imaging system," *IEEE Trans. Microwave Theory Tech.*, vol. MTT-24, pp. 786–793, Nov. 1976.

[2] R. P. Moore, "Real-time microwave radiometric imager," *Proc. Soc. of Photo-Optical Instrum. Eng.*, pp. 60–66, 1977.

[3] B. Vowinkel, J. K. Peltonen, W. Reinert, K. Grüner, and B. Aumiller, "Airborne imaging system using a cryogenic 90 GHz receiver," *IEEE Trans. Microwave Theory Tech.*, vol. MTT-29, pp. 535–541, June 1981.

[4] J. A. Gagliano and W. Gregorwich, "High-altitude atmospheric measurements at 92/183 GHz onboard the ER-2 research aircraft," in *Proc. Eighth Int. Conf. on Infrared and Millimeter-waves*, 1983, p. M 6.8.

[5] A. W. Rudge and N. A. Adatia, "Offset-parabolic-reflector antennas: A review," *Proc. IEEE*, vol. 66, pp. 1592–1618, Dec. 1978.

[6] J. W. M. Baars, "Characteristics of the paraboloidal reflector antenna," NRAO Electronics Division Internal Report, no. 57, Aug. 1966.

✠

William J. Wilson (M'80–SM'86) was born in Spokane, WA, on December 16, 1939. He received the B.S.E.E. degree from the University of Washington, Seattle, in 1961, and the M.S.E.E., E.E., and Ph.D. degrees in electrical engineering from the Massachusetts Institute of Technology, Cambridge, in 1963, 1964, and 1970, respectively.

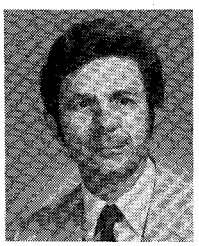

From 1964 to 1967, he served in the U.S. Air Force, working on military communication satellites. In 1970, he joined the Aerospace Corporation, Los Angeles, CA, and was involved in the design and construction of millimeter-wave receivers and radio astronomy observations. In 1976/77, he was an Assistant Professor in the Electrical Engineering Department at the University of Texas at Austin. He returned to Aerospace in 1977, where he was involved with research in millimeter-wave radiometers and low-noise receivers. In 1980, he joined the staff of NASA's Jet Propulsion Laboratory, Pasadena, CA, and is the Supervisor of the Microwave Advanced Systems Group. At JPL, he has been working on low-noise millimeter-wave and submillimeter-wave radiometers and systems for spacecraft instruments and earth remote sensing applications.

✠

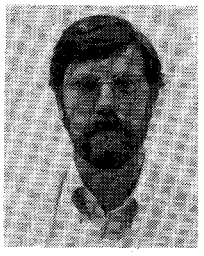

R. J. Howard (M'85) received the B.S. degree in physics and astronomy from the University of Wisconsin in 1968, and the M.S. degree in astronomy from the Pennsylvania State University in 1974.

He was employed by the National Radio Astronomy Observatory from 1975 to 1984 as an electronics engineer working on millimeter-wave receivers and antenna performance. He worked at the Jet Propulsion Laboratory from 1984 to 1986 as a member of the Technical Staff on advanced microwave and millimeter-wave remote sensing systems. He is currently the Technical Manager of the Caltech Submillimeter Observatory, located in Hawaii.

✠

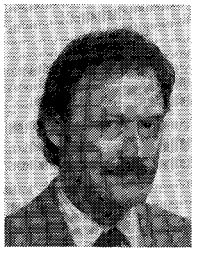

Anthony C. Ibbott was born in Kent, England, in 1953. In 1973, he received an associate science degree in computer science from Pierce College, and in 1981, a bachelor of arts in management from the University of Redlands, both in California. He began working with computers in 1971 on data reduction applications at Bio-Science Laboratories and in 1978 became involved in data processing for Zero Corporation.

In 1981, he joined the Jet Propulsion Laboratory in Pasadena, CA. As a computer analyst at JPL, he has created software to monitor, control, collect, and analyze data from very long baseline interferometry stations, water vapor radiometers, and, currently, data acquisition and image processing for the millimeter-wave radiometer.

✠

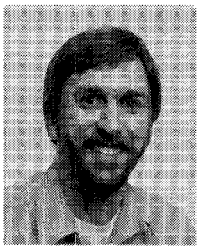

Gary S. Parks was born in Pasadena, CA, on May 8, 1953. He received a B.S. degree in electrical engineering from the California Polytechnic State University in 1976.

From 1976 to 1983, he worked as an electrical engineer for NASA's Jet Propulsion Laboratory, Pasadena, CA, on instrumentation for ground-based geodetic applications of very long baseline interferometry techniques. In 1983, he joined the staff of the Jet Propulsion Laboratory and has been working on the Unmanned Aerial Vehicle project and on advanced microwave and millimeter-wave remote sensing systems.

✠

William B. Ricketts was born in Los Angeles, CA, on February 5, 1929. He attended Santa Monica College and the University of California at Los Angeles. He is also a graduate of the U.S. Air Force Electronics and Advanced Radar School, Biloxi, MS.

From 1952 to 1958, he served as Senior Microwave Field Engineer for Gilfillan Bros., and was responsible for the installation and operation of ground controlled approach radar stations in both the United States and Europe. He was employed from 1958 to 1960 as a Research Assistant in the Falcon Missile Receiver Group at Hughes Aircraft. In 1960, he joined Aerojet Electrosystem Co., as a Senior Engineer in the Microwave Systems Dept., and participated in the design and development of numerous airborne microwave radiometers. Since 1975, he has been on the staff of the Jet Propulsion Laboratory in Pasadena, CA. At JPL, he has been involved with the design and development of millimeter- and submillimeter-wave radiometer systems.